Time-domain Differential Protection Based on Operating and Restraining Trajectory Indices for Lines Connecting Battery Storage Energy Stations

Yingyu Liang and Cunyue Pan

***Abstract*—Battery energy storage stations (BESSs) pose several challenges for both phasor-based differential protection and the newly-proposed time-domain differential protection. These challenges include low sensitivity and even rejection. Besides, the negative impact of various nonideal conditions, including current transformer (CT) saturation, errors, and outliers, on the security of differential protection remains an important problem. Motivated by the aforementioned issues, this study accounts for the trajectory distribution discrepancy on Cartesian plane under various conditions and proposes a time-domain differential protection method. In this paper, the trajectory formed by operating and restraining current samples is developed. Subsequently, after considering different operating states, the fault severity levels, and nonideal conditions, the variances in trajectory distribution between internal and external faults are extensively analyzed. On this basis, the Cartesian plane is divided into operating, uncertainty, and restraining zones. Further, the operating and restraining trajectory indices are meticulously designed and a protection criterion based on these indices is formed to accurately separate internal faults from other events, unaffected by CT saturation, errors, and outliers. The exceptional performance of the proposed protection method is extensively validated through PSCAD simulations and a hardware-in-the-loop testing platform. Regarding the dependability, sensitivity, and security, the proposed protection method outperforms three state-of-the-art differential protection methods.**

***Index Terms*—Battery energy storage station, time-domain differential protection, operating trajectory index (OTI), restraining trajectory index (RTI).**

I. Introduction

FOR achieving carbon neutrality, the penetration rate of renewable energy is continuously and rapidly increasing and will eventually displace thermal power as the main source in power systems [1]. Nevertheless, some inherent defects of renewable energy such as volatility, randomness, and intermittency undermine its stability and frequency quality in the power grid. The battery energy storage stations (BESSs) play a crucial role in mitigating the adverse effects of power fluctuations inherent in renewable energy sources [2]-[4]. In fact, BESSs will be essential for future power grids dominated by renewable energies.

Despite its benefits, the BESS presents certain challenges to the reliability of conventional relay protection that depends on the fault behaviors of synchronous generators (SGs). To improve the performance of power frequency component based conventional current differential protection (CDP), two time-domain differential protection (TDDP) methods for lines connecting SGs are proposed in [5] and [6]. These protection methods use the cosine similarity coefficient (CSC) and Hausdorff distance to evaluate the similarity between the current waveforms on both sides, accurately distinguishing the internal and external faults. However, the fault behaviors of the BESS are neglected. Consequently, the protection methods in [5] and [6] may suffer from a low sensitivity or even malfunction in the presence of a BESS.

Photovoltaic power, wind power, voltage source converter based high-voltage direct current (VSC-HVDC) stations, and BESSs are power electronic-based power sources. Compared with SGs, they share some common fault behaviors. Thus, we consider protection methods of lines connecting renewable energy plants and VSC-HVDC stations as a reference. In [7]-[9], the phasor-based differential protection methods are proposed based on communication channels, but they are not phase-segregated, impeding to identify the faulty phase. To circumvent this drawback, some phase-segregated time-domain protection methods have recently been proposed for lines connecting renewable energy plants. These methods are based on the Pearson correlation coefficient [10], CSC [11], [12], fault detection index (FDI) [13], improved Euclidean distance [14], and signed correlation index [15]. In [10]-[15], the transient fault current characteristics of renewable energy plants are fully considered, and the protection methods adapt to the presence of renewable energy plants. Renewable energy plants convert wind and solar energy into electricity, which is then delivered to the power grid. Consequently, renewable energy plants operate in the inverter state. Unlike these plants, a BESS can operate in charging and discharging states, thereby increasing the operating range and intricacy of fault characteristics. Thus, the fault behaviors of BESS considerably differ from those of renewable energy plants.

Manuscript received: August 31, 2023; revised: October 7, 2023; accepted: November 28, 2023. Date of CrossCheck: November 28, 2023. Date of online publication: February 6, 2024.

This work was supported in part by the National Natural Science Foundation of China (No. 52277132) and in part by the Fundamental Research Funds for the Central Universities (No. 2024JCCXJD01).

Y. Liang (corresponding author) and C. Pan are with the School of Mechanical and Electrical Engineering, China University of Mining and Technology (Beijing), Beijing, China (e-mail: liangyingyu2013@163.com; pancunyue@163.com).

DOI: 10.35833/MPCE.2023.000618

The design of the protection methods in [7]-[15] is specifically tailored to the fault characteristics of renewable plants, resulting in potential performance degradation or even failure to operate properly when confronted with BESSs.

Both the VSC-HVDC station and BESS can operate under the charging (rectifier) and discharging (inverter) states. Thus, they share more common fault behaviors compared with renewable energy plants. The performance difference of conventional CDP between the rectifier and inverter states is analyzed in [16]. To improve the protection reliability in the rectifier state, an enhanced CDP is introduced. Compared with the phasor-based protection, the time-domain protection removes the phasor estimation based on discrete Fourier transform, thus reducing the computational burden. In [17], dual differential currents are used to propose a time-domain line protection for VSC-HVDC stations with a low complexity. Although the protection method in [17] provides robustness to outliers and current transformer (CT) saturation, its response speed should be further improved. Compared with renewable energy plants and VSC-HVDC stations, scarce research on protection methods for lines connecting BESSs is available. A conventional directional protection method may maloperate in the presence of a BESS [18]. To address this problem, a new direction estimation method is presented in [18], but it still requires phasor estimation and is not phase-segregated. To eliminate phasor estimation, an internal fault probability-based time-domain protection method is proposed in [19]. Nevertheless, the negative effects of CT errors remain unconsidered. Based on the time-domain fault current characteristics under the charging and discharging states of a BESS, a current trajectory coefficient (CTC) based time-domain protection method is proposed in [20]. However, this method may suffer from low sensitivity, and its performance is affected by the BESS capacity. In addition to sensitivity, the speed is also an important factor in relay protection. Fast fault clearance improves transient stability, particularly in power systems dominated by power electronic-based sources. Therefore, a time-domain protection method that exhibits high sensitivity, rapid response, and excellent tolerance towards CT saturation, errors, and outliers must be devised for BESS-integrated power systems.

The main contributions of this paper are summarized as follows.

1) The concept of the current trajectory formed by time-domain operating and restraining current samples is developed. The divergence in the distribution patterns of the current trajectories on a Cartesian plane under various conditions is investigated, establishing a fundamental basis for the proposal of a novel time-domain protection method.

2) After considering the distribution patterns of current trajectories under various conditions, the Cartesian plane is divided into five zones. The methodology for this division and the principles for selecting the key parameters are detailed.

3) The operating trajectory index (OTI) and restraining trajectory index (RTI) are designed. Furthermore, a TDDP method based on the OTI and RTI is proposed, which does not require discrete Fourier transform.

4) The excellent functionality of the proposed protection method is extensively validated using PSCAD simulations and a hardware-in-the-loop (HIL) testing platform. The proposed method functions well across a variety of fault types, resistances, locations, and operating states of a BESS, outperforming state-of-the-art time-domain protection methods.

The remainder of this paper is organized as follows. Section II describes the potential problems of phasor-based CDP. In Section III, the trajectory distribution discrepancy under various conditions is analyzed in detail, and the division principles of the operating, uncertainty, and restraining zones are described and derived. Furthermore, a protection criterion based on the OTI and RTI is designed. The exceptional performance of the proposed protection method is extensively validated, and a comparative study with some newly-proposed TDDP methods is conducted in PSCAD software and HIL testing platform in Sections IV and V, respectively. Section VI discusses future work and explores new trends. In Section VII, we draw conclusions.

II. Potential Problems of Phasor-Based CDP

A modified 230 kV 50 Hz IEEE 39-bus system with a BESS is considered, as shown in Fig. 1. The BESS with a capacity of 250 MW is integrated into the grid via a 50 km line (line 33-19). i_g and i_b are the currents on the grid side and BESS side, respectively; and $\dot{I}_b$ and $\dot{I}_g$ are the corresponding phasors. As shown in Fig. 1(b), the parameters of line 33-19 can be found in [17], and PT is short for potential transformer.

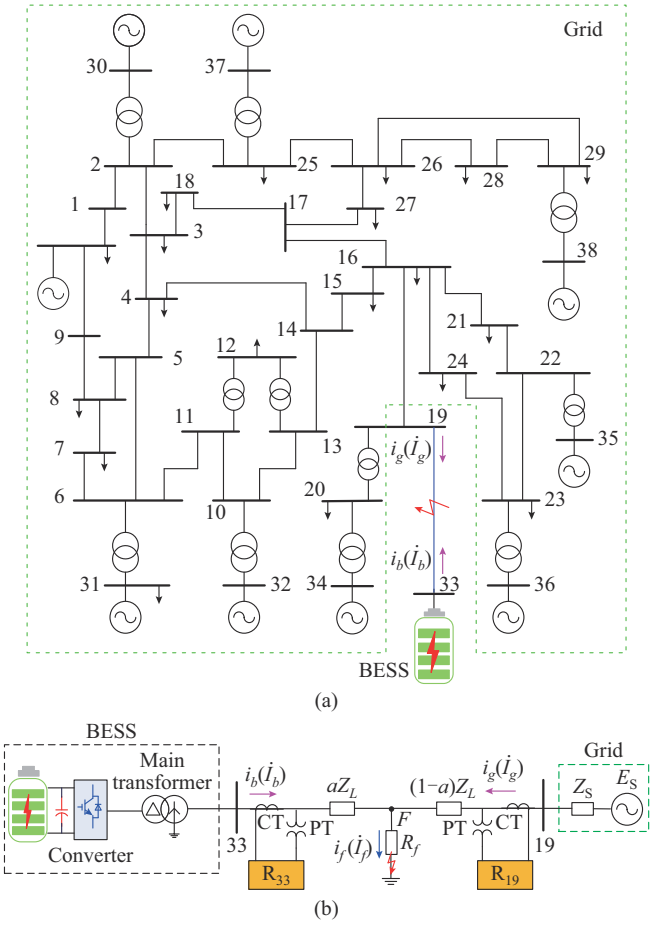

Fig. 1. IEEE 39-bus system with BESS. (a) Detailed model. (b) Simplified model.

Because of its absolute selectivity and speed, the phasor-based CDP is always the first choice for primary protection of transmission lines in conventional power systems. Its operating criterion is given by:

$$\underbrace{\left|\dot{I}_b+\dot{I}_g\right|}_{|\dot{I}_{op}|} \geq K \underbrace{\left|\dot{I}_b-\dot{I}_g\right|}_{|\dot{I}_{res}|} \tag{1}$$

where $\dot{I}_{op}$ and $\dot{I}_{res}$ are the operating and restraining currents, respectively; and K is the restraining coefficient with a value usually between 0.5 and 0.8.

The potential problems with phasor-based CDP can be divided into two categories. The first category is dependability issue caused by the presence of a BESS under an internal fault. The second category is a security issue caused by nonideal conditions during external faults, such as CT saturation, errors, and outliers.

To illustrate the potential problems, (1) is rewritten as:

$$|1+\lambda| \geq K|1-\lambda| \tag{2}$$

where λ is a complex number given by:

$$\lambda=\frac{\min\left(\dot{I}_b,\dot{I}_g\right)}{\max\left(\dot{I}_b,\dot{I}_g\right)}=a+\mathrm{j}b \tag{3}$$

where a and b are the real and imaginary parts of λ, respectively.

Based on (2) and (3), the following function is derived as:

$$f(a,b)=\sqrt{(1+a)^2+b^2}-K\sqrt{(1-a)^2+b^2} \tag{4}$$

When $f(a,b)>0$, the operating criterion expressed as (2) is satisfied, thus indicating an internal fault.

When $f(a,b)<0$, the operating criterion is not satisfied, thus indicating an external fault. $f(a,b)=0$ corresponds to the critical operating state.

In Fig. 2, the blue, black, and red curves represent the boundary lines between the operating and restraining zones for $K=0.5$, 0.6, and 0.8 when $f(a,b)=0$, respectively. The range of the operating zone is negatively correlated with K, whereas that of the restraining zone is positively correlated with K. Therefore, a large K indicates high security and low dependability, whereas a small K indicates low security and high dependability. For phasor-based CDP, an inherent trade-off exists between the dependability and security. Considering this trade-off, K is taken as 0.65 (i.e., the average of 0.5 and 0.8) to elucidate potential problems of CDP.

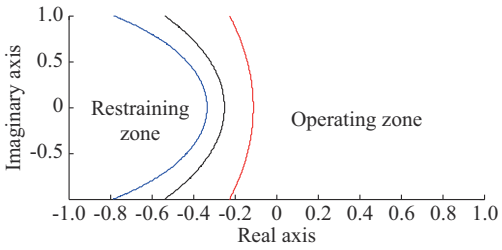

Fig. 2. Operating and restraining zones under different restraining coefficients.

A. Dependability Problem

To illustrate the dependability problem of CDP, an internal fault with a fault resistance of 50 Ω is considered. Figure 3 shows the dynamic trajectory of λ in the discharging and charging states. When the BESS is in the discharging state, the dynamic trajectory of λ moves into the operating zone. Consequently, the relay operates correctly to clear this fault. When the BESS is in the charging state, the dynamic trajectory of λ remains within the restraining zone, and thus the relay fails to operate effectively. Compared with the discharging state, CDP is more likely to suffer from the dependability problem in the charging state of BESS.

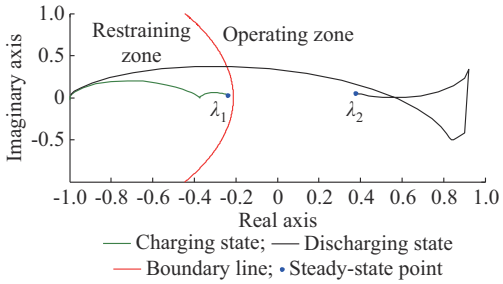

Fig. 3. Dynamic trajectory of λ in different operating states.

In the steady state, $\lambda_1 \approx -0.239+\mathrm{j}0.026$ in the charging state, and $\lambda_2 \approx 0.376+\mathrm{j}0.056$ in the discharging state. The magnitude of the real part substantially exceeds that of the imaginary part. Thus, the angle of λ approaches 0° and 180° in the discharging and charging states, respectively. This indicates that the currents at the ends are in phase in the discharging state and out of phase in the charging state. When a short-circuit fault occurs, the SG generally exhibits feed-in characteristics by feeding current to the fault point. Thus, when the BESS operates in the discharging state, both the SG and BESS exhibit feed-in characteristics that are similar to the fault behaviors of conventional power systems. However, when the BESS operates in the charging state, the fault currents of the SG and BESS are out of phase. Consequently, the BESS presents the opposite characteristic to the SG, i.e., a draw-out characteristic. In other words, the BESS draws current from the fault point. The different fault characteristics in the charging and discharging states lead to drastically different operating performances of CDP.

B. Security Problem

In this subsection, three typical nonideal conditions are considered as follows.

1) CT error: the CT on the grid side has a measurement error of −10% during an external fault.

2) CT saturation: the CT on the grid side is saturated during an external fault.

3) Outliers: the outliers are introduced into the measured current on the BESS side during an external fault.

Figure 4 shows the dynamic trajectories of λ during external faults under the three nonideal conditions. The black curve always remains inside the restraining zone and is far from the boundary line. This implies that CDP is robust against CT errors. In contrast, the blue and green curves enter the operating zone. Consequently, the corresponding fault

is erroneously judged to occur within the protection zone, leading to the unwanted operation of CDP. Thus, the CT saturation and outliers notably deteriorate the security of CDP, which should be addressed.

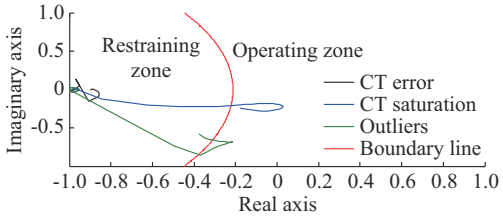

Fig. 4. Dynamic trajectories of λ during external faults under three nonideal conditions.

III. Time-domain CDP Based on Trajectory Distribution Discrepancy

A. Current Trajectory Formed by Time-domain Operating and Restraining Currents

Considering the shortcomings of phasor-based CDP in the presence of a BESS, we propose a time-domain CDP. Time-domain current arrays on both sides are composed of current samples, which are expressed as:

$$\boldsymbol{i}_b=\left[i_b(k)\quad i_b(k-1)\quad \cdots\quad i_b(k-N+1)\right] \tag{5}$$

$$\boldsymbol{i}_g=\left[i_g(k)\quad i_g(k-1)\quad \cdots\quad i_g(k-N+1)\right] \tag{6}$$

where N is the length of the data window.

Similar to phasor-based CDP, the time-domain operating and restraining current arrays $\boldsymbol{i}_{op}$ and $\boldsymbol{i}_{res}$ are defined as:

$$\boldsymbol{i}_{op}=\boldsymbol{i}_b+\boldsymbol{i}_g=\left[i_{op}(k)\quad i_{op}(k-1)\quad \cdots\quad i_{op}(k-N+1)\right] \tag{7}$$

$$\boldsymbol{i}_{res}=\boldsymbol{i}_b-\boldsymbol{i}_g=\left[i_{res}(k)\quad i_{res}(k-1)\quad \cdots\quad i_{res}(k-N+1)\right] \tag{8}$$

$$\begin{cases} i_{op}(k)=i_b(k)+i_g(k) \\ i_{res}(k)=i_b(k)-i_g(k) \end{cases} \tag{9}$$

As shown in Fig. 5, the operating and restraining current samples are mapped to the x-axis and y-axis on a Cartesian plane, respectively. After all the samples in (7) and (8) are mapped to the Cartesian plane, a current trajectory composed of time-domain operating and restraining current arrays is formed, as shown in Fig. 5. In fact, the current trajectory on the Cartesian plane contains all the fault current information at both ends. Thus, the trajectory formed by the operating and restraining currents can be employed to distinguish internal faults from other events. The key lies in how to effectively utilize current trajectory characteristics to accommodate the presence of BESS and various nonideal conditions.

B. Description and Analysis of Current Trajectory Distribution Characteristics on Cartesian Plane

1) Normal Conditions and Internal Faults

To separate the internal faults from normal condition, the divergence in the trajectory distribution characteristics between these conditions should be analyzed.

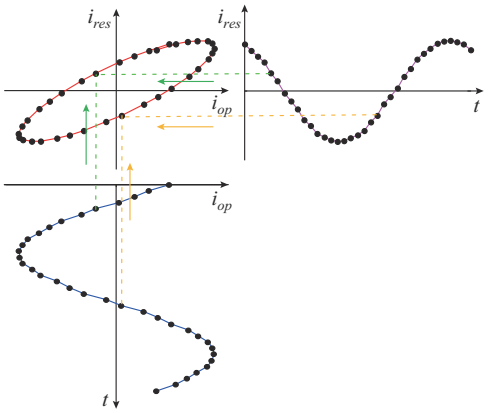

Fig. 5. Schematic diagram of current trajectory formation.

Under normal conditions, the operating current approaches zero and is substantially lower than the restraining current. Thus, the current trajectory is close to y-axis, as shown in Fig. 6(a) and (b). When a severe internal fault occurs, owing to the weak infeed of the BESS, i_g is considerably larger than i_b regardless of the charging or discharging state.

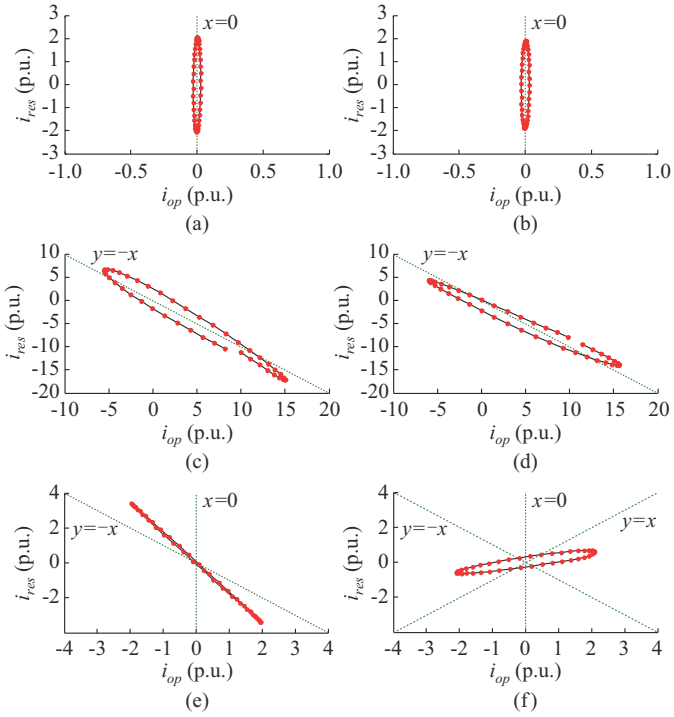

Fig. 6. Current trajectories on Cartesian plane under normal condition and internal faults. (a) Normal condition (charging state). (b) Normal condition (discharging state). (c) Severe internal fault (charging state). (d) Severe internal fault (discharging state). (e) High-resistance internal fault (charging state). (f) High-resistance internal fault (discharging state).

Thus, we have:

$$\begin{cases} i_{op}(m)=i_b(m)+i_g(m)\approx i_g(m) \\ i_{res}(m)=i_b(m)-i_g(m)\approx -i_g(m) \end{cases} \Rightarrow i_{op}(m)\approx -i_{res}(m) \tag{10}$$

where $m=k,k-1,\ldots,k-N+1$.

According to the approximation relation in (10), the current trajectory should be around $y=-x$, as confirmed in Fig.

6(c) and (d).

As the fault resistance increases, the current trajectory gradually deviates from $y=-x$. As shown in Fig. 6(e) and (f), when high-resistance internal faults occur, the current trajectory clearly deviates from $y=-x$. The disparity between the normal condition and the internal fault in the current trajectory is clear. Therefore, the trajectory formed by the time-domain operating and restraining currents can serve as a sensitive means of distinguishing internal faults from normal condition.

2) External Faults

For the precise identification of whether the fault occurs within or outside the protection zone, the trajectory distribution characteristics of the external fault and the difference with those of internal faults should be investigated. To improve the robustness and minimize the impact of CT saturation, errors, and outliers, the three abovementioned nonideal conditions are considered.

Figure 7(a) shows the current trajectory of the external fault without nonideal conditions. The trajectory is very similar to that under normal condition shown in Fig. 6(a). As observed from Fig. 7(b), although the outliers have great influence on the shape of the current trajectory, it is still considerably different from Fig. 6(c)-(f). In Fig. 7(b), most of the trajectory points remain near the y-axis. Figure 7(c) and (d) shows the current trajectories in the presence of a CT error. Under an external fault, the currents at both ends are approximated as:

$$i_b(m) \approx -i_g(m) \tag{11}$$

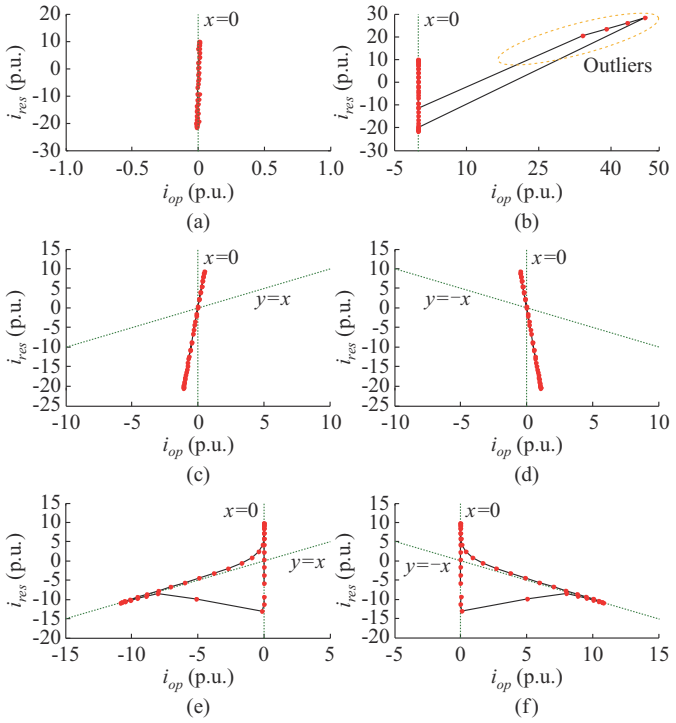

Fig. 7. Current trajectories on Cartesian plane under external faults and three nonideal conditions. (a) External fault. (b) Outliers. (c) −10% CT error on grid side. (d) −10% CT error on BESS side. (e) CT saturation on grid side. (f) CT saturation on BESS side.

Considering a CT error of $-\varepsilon$ on the grid side, the operating and restraining currents can be expressed as:

$$\begin{cases} i_{op}(m) \approx -\varepsilon i_g(m) \\ i_{res}(m) \approx -(2-\varepsilon) i_g(m) \end{cases} \tag{12}$$

Thus, we have:

$$\frac{i_{res}(m)}{i_{op}(m)} \approx \frac{2-\varepsilon}{\varepsilon} > 0 \tag{13}$$

When $\varepsilon = 10\%$, i_{res}/i_{op} is approximately 19, being a positive value. Therefore, the current trajectory exhibits a steep slope in the first and third quadrants, being consistent with the trajectory shown in Fig. 7(c).

When a measurement error of $-\varepsilon$ is introduced into the CT on the BESS side, a similar derivation occurs. The following relation is obtained as:

$$\frac{i_{res}(m)}{i_{op}(m)} \approx -\frac{2-\varepsilon}{\varepsilon} < 0 \tag{14}$$

When $\varepsilon = 10\%$, i_{res}/i_{op} is approximately −19, being a negative value. Therefore, the current trajectory shows a high slope in the second and fourth quadrants, being consistent with the trajectory shown in Fig. 7(d).

For differential protection, the CT saturation always bring great challenges to its security. In the linear transferring zone of CT, the currents on both sides satisfy the relation in (11). Thus, the operating current is close to zero. Part of the current trajectory is near y-axis. When the CT enters the saturation zone, the current trajectory deviates considerably from y-axis. As shown in Fig. 7(e) and (f), the current trajectory in the linear transferring zone of the CT is near y-axis, while that in the saturation zone of the CT approaches $y=x$ or $y=-x$.

By carefully comparing and analyzing Fig. 6(c)-(f) and Fig. 7(a)-(f), the current trajectories under various external faults are notably different from those under various internal faults. Therefore, the trajectory formed by the operating and restraining currents allows to precisely identify whether the fault occurs within or outside the protection zone. Accordingly, we propose a time-domain CDP method based on the discrepancy in current trajectory distribution characteristics.

C. Principle and Protection Criterion of Time-domain CDP Based on Discrepancy of Current Trajectory

1) Division Principle of Operating, Uncertainty, and Restraining Zones

We analyze the discrepancy in the current trajectory distribution on the Cartesian plane under various circumstances, i. e., normal conditions, internal faults, and external faults with and without nonideal conditions. Then, the Cartesian plane is divided into five zones, as shown in Fig. 8.

Zones 1-4 can be determined by (15a)-(15d), respectively.

$$|x| < I_{th} \tag{15a}$$

$$\left(|x| \geq I_{thr}\right) \cap \left\{\left(\beta < ATAN2D(y,x) < 180° - \beta\right) \cup \left(-180° + \beta < ATAN2D(y,x) < -\beta\right)\right\} \tag{15b}$$

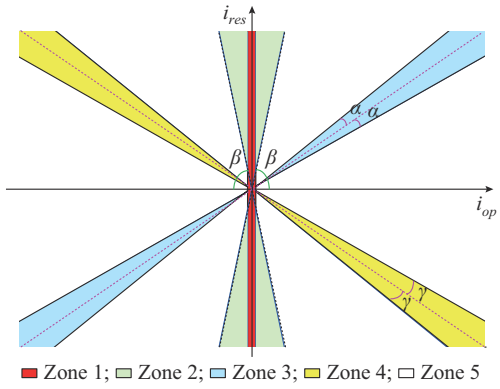

Fig. 8. Schematic of partition on Cartesian plane.

$$\left(|x|\geq I_{th}\right)\cap\left\{\left(45°-\alpha<ATAN2D\left(y,x\right)<45°+\alpha\right)\cup\left(-135°-\alpha<ATAN2D\left(y,x\right)<-135°+\alpha\right)\right\} \tag{15c}$$

$$\left(|x|\geq I_{th}\right)\cap\left\{\left(135°-\gamma<ATAN2D\left(y,x\right)<135°+\gamma\right)\cup\left(-45°-\gamma<ATAN2D\left(y,x\right)<-45°+\gamma\right)\right\} \tag{15d}$$

where $ATAN2D\left(y,x\right)=\arctan\left(y/x\right)$ and ranges from $-180°$ to $180°$; I_{th} is the current threshold; and β, α, and γ determine the sizes of zones 2-4, respectively.

Considering the trajectory analysis under diverse conditions in Section III-B, zones 1-3 are designated as restraining zone, zone 4 is designated as the uncertainty zone, and zone 5 is designated as the operating zone.

Under normal conditions, external faults without nonideal conditions, and the linear transferring zone of the CT, the trajectory points are expected to fall into zone 1. Hence, I_{th} should be greater than the line capacitive current:

$$I_{th}\geq U_n\omega_n Cl \tag{16}$$

where U_n is the rated voltage; ω_n is the rated angular frequency; C is the capacitance per unit length; and l is the line length. For a 230 kV transmission line, its length typically does not exceed 300 km. Hence, in this paper, l is set to be 300 km.

As shown in Fig. 8, β determines the size of zone 2. The principle for selecting β is ensuring the robustness against a CT error. Suppose that the grid side has a CT error of $-\varepsilon$ and the BESS side has a CT error of ε. To ensure that most of the current trajectory points fall into zone 2, the following relation should be satisfied:

$$\beta\leq\arctan\frac{y}{x}=\arctan\frac{i_{res}}{i_{op}}=\arctan\frac{i_b-i_g}{i_b+i_g}\approx\arctan\frac{-(1+\varepsilon)i_g-(1-\varepsilon)i_g}{-(1+\varepsilon)i_g+(1-\varepsilon)i_g}=\arctan\frac{1}{\varepsilon} \tag{17}$$

The value of β clearly depends on the CT error ε. To ensure the robustness against CT errors, we consider a worst-case scenario of ε being a large value of 10%. In this case, β is approximately less than or equal to 84°. Considering 2° as a margin, β is set to be 82°.

Under an external fault, when the CT on the grid side is saturated (see Fig. 7(e)), most of the trajectory points should be inside zones 1 and 3. To facilitate the theoretical analysis, the generalized saturated current waveform of CT in [21] is introduced. Once the CT starts to saturate, the secondary current of CT instantaneously becomes zero. When the CT on the grid side is not saturated, we can obtain:

$$x=i_{op}=i_b+i_g\approx-i_g+i_g=0 \tag{18}$$

Thus, the points corresponding to the unsaturated zone of CT can easily fall into zone 1. When the CT on the grid side is saturated, i_g is considered to instantaneously become zero, as stated in [21]. Thus, we have:

$$\begin{cases}x=i_{op}=i_b+i_g=i_b\\y=i_{res}=i_b-i_g=i_b\end{cases}\Rightarrow y=x \tag{19}$$

From (19), most of the points corresponding to the saturated zone of the CT are very close to $y=x$. Zone 3 is the zone with the symmetry axis of $y=x$, and α determines the size of zone 3. Because the points associated with the saturated zone of the CT theoretically lie on the $y=x$, a relatively small α value (e.g., 5°) is generally sufficient for most of the points corresponding to the saturated zone to fall into zone 3.

As shown in Fig. 8, γ determines the size of zone 4. The value of γ is selected to ensure that the trajectory points associated with the saturated zone of the CT on the BESS side fall into zone 4. When the CT on the BESS side saturates, i_b is considered to instantaneously become zero. Hence, the following relations can be derived as:

$$\begin{cases}x=i_{op}=i_b+i_g=i_g\\y=i_{res}=i_b-i_g=-i_g\end{cases}\Rightarrow y=-x \tag{20}$$

From (20), the points associated with the saturated zone of the CT theoretically lie on the $y=-x$. Thus, in theory, γ can be assigned the identical value as α, i.e., $\gamma=\alpha=5°$. However, when a severe internal fault occurs, some trajectory points may also fall into zone 4, as shown in Fig. 6(c) and (d). Hence, zone 4 is an uncertainty zone. Compared with Fig. 6(c) and (d), the trajectory points in the saturation zone of the CT on the BESS side are close to $y=-x$, as shown in Fig. 7(f). Hence, in order that as many trajectory points as possible in Fig. 6(c) and (d) do not fall into the zone 4, γ should be set to be a very small value less than α (i. e., $\gamma<\alpha$). There is no harm to consider a margin of 2°. Therefore, γ can be chosen as 3° in this paper.

2) Protection Criterion

A variable $\chi(m)$ is defined to describe the location of the trajectory point as:

$$\chi(m)=\eta\quad\left(i_{op}(m),i_{res}(m)\right)\in\text{zone}\,\eta, m=k,k-1,\ldots,k-N+1 \tag{21}$$

where $\eta=1,2,\ldots,5$.

The variable $p_\eta(m)$ is defined to indicate whether the trajectory point is inside zone η as:

$$p_\eta(m)=\begin{cases}1 & \chi(m)=\eta\\0 & \chi(m)\neq\eta\end{cases} \tag{22}$$

It is clear that the variable $p_\eta(m)$ can indicate the distribution discrepancy of the current trajectory on the Cartesian plane between an internal fault and other disturbances. Thus, if $p_\eta(m)$ is used properly, an internal fault can be accurately distinguished from other events.

Considering the distribution discrepancy of the current trajectory under diverse conditions, the OTI of time-domain CDP is defined as:

$$OTI = \frac{1}{N}\left(\sum_{m=k-N+1}^{k} p_5(m) + \mu \sum_{m=k-N+1}^{k} p_4(m) \right) \tag{23}$$

where μ is a weight satisfying $0 < \mu < 1$.

The RTI can be chosen as a constant. An internal fault is identified when the OTI exceeds the RTI. A large RTI leads to high security but low sensitivity and dependability, while a small RTI results in high sensitivity and dependability but low security. To simultaneously achieve high security and sensitivity, the RTI is designed as the summation of a small constant and varying quantity f_q:

$$RTI = 0.2 + f_q \tag{24}$$

Regardless of normal condition, external faults without nonideal conditions, and external faults with outliers and CT saturation, there is always a considerable number of trajectory points falling into zone 1. On the other hand, few trajectory points are located inside zone 1 under various internal faults. Therefore, the number of trajectory points inside zone 1 can be used to design the varying quantity f_q. The RTI can be rewritten as:

$$RTI = 0.2 + \frac{1}{N} \sum_{m=k-N+1}^{k} p_1(m) \tag{25}$$

The protection criterion for an internal fault is expressed as:

$$OTI > RTI \tag{26}$$

In general, RTI approaches 0.2 under internal faults, resulting in high sensitivity. Under external faults, since a considerable number of trajectory points are located in zone 1, the RTI is relatively large, resulting in high security.

Considering the extreme case, all the trajectory points in Fig. 6(c) and (d) are inside the uncertainty zone (i.e., zone 4) under an internal fault. In this case, the OTI is approximately μ, and the RTI is approximately 0.2. To ensure that OTI is larger than RTI in this case, μ is chosen as a number slightly larger than 0.2 (e.g., 0.25), which can avoid a large OTI and assure high security in the case of external fault with CT saturation on the BESS side. In fact, due to a very small γ, it is impossible that all trajectory points in Fig. 6(c) and (d) are inside zone 4. The points in the operating zone further increase the OTI value. Thus, a μ value of 0.25 is sufficient. In addition, it is worth mentioning that the RTI should not exceed 1.

D. Implementation of Proposed Protection Method

The proposed protection method is implemented, as shown in Fig. 9.

Step 1: obtain current samples on both sides.

Step 2: if a fault is detected, go to the next step. Otherwise, set $p_\eta(m)$ to zero and return to *Step 1*. For fault detection, refer to [5].

Step 3: calculate variable $p_\eta(m)$.

Step 4: calculate the OTI and RTI using (23) and (25), respectively.

Step 5: if OTI surpasses RTI, the fault is considered to occur within the protection zone. Thus, the relay generates the tripping signal. Otherwise, the fault is considered to be outside the protection zone, i.e., an external fault.

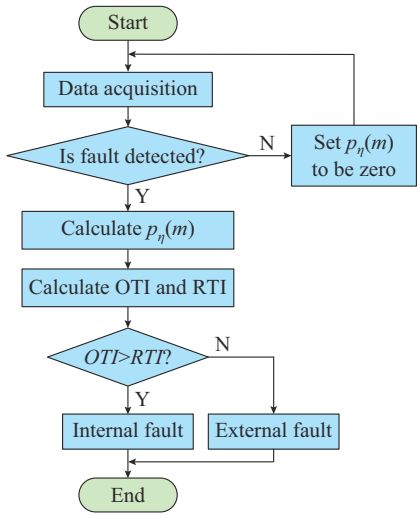

Fig. 9. Flowchart of proposed protection method.

IV. Performance Evaluation Using PSCAD

To verify the effectiveness and assess the performance of the proposed protection method, the modified 39-bus system with a BESS shown in Fig. 1(a) is built in the PSCAD. A sampling rate of 4 kHz is employed in this section.

A. Capability Against Fault Resistance

Given that short-circuit faults commonly involve fault resistance, the capability to withstand a fault resistance serves as a crucial indicator to measure the performance of relay protection. To assess the capability of proposed protection method against fault resistance, AG faults with varying fault resistances are introduced at $t = 1$ s at the midpoint of line 33-19. The fault resistance values include 1 Ω, 50 Ω, and 100 Ω, covering a broad spectrum. Furthermore, both charging and discharging states of BESS are considered.

The simulation waveforms of the OTI and RTI with different fault resistances are shown in Fig. 10(a)-(c). The OTI always exceeds the RTI within 10 ms after the fault occurrence regardless of the variations in the fault resistance and operating state of the BESS. According to the criterion given by (26), this implies that the proposed protection method can quickly and precisely identify internal faults. The simulation results corroborate the excellent capability of the proposed method to tolerate a fault resistance and provide a rapid response.

B. Different Fault Locations and Types

To comprehensively evaluate the proposed protection method, several internal faults are applied considering different fault locations and types. The fault types include BG, AB, BCG, and ABC. Three fault locations, designated as F1, F2, and F3, are placed at 10%, 50%, and 90% of the distance from bus 33 to bus 19, respectively. The BESS operates in the charging state, and the fault resistance is set to be 30 Ω.

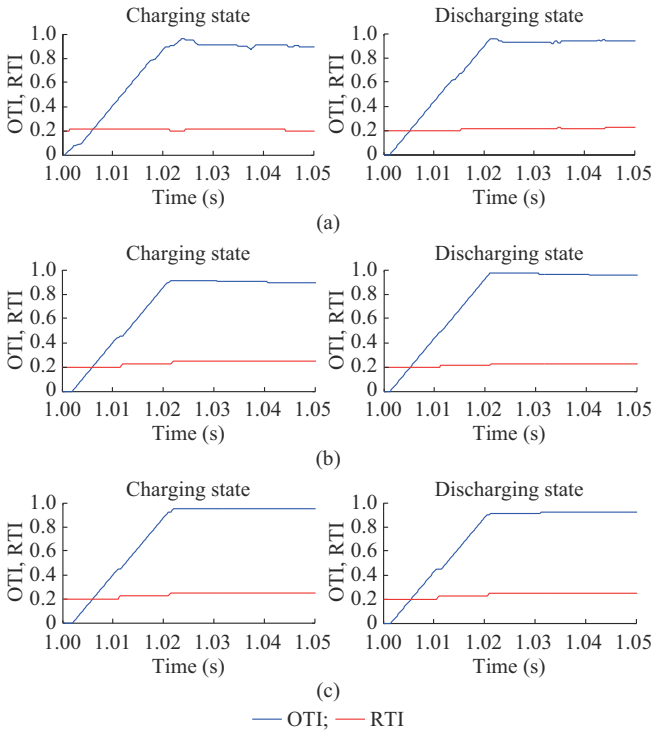

Fig. 10. Simulation waveforms of OTI and RTI with different fault resistances. (a) 1 Ω. (b) 50 Ω. (c) 100 Ω.

The OTI and RTI under different fault types and locations are listed in Table I. The OTI consistently exceeds the RTI by a large margin for the faulty phases, whereas the OTI consistently remains notably lower than the RTI for the healthy phases. Hence, the proposed protection method can correctly identify faults within the protection zone and precisely identify the faulty phases with high sensitivity.

TABLE I
OTI AND RTI UNDER DIFFERENT FAULT TYPES AND LOCATIONS

Fault location	Fault type	Phase A		Phase B		Phase C	
		OTI	RTI	OTI	RTI	OTI	RTI
F1	BG	0	1	0.769	0.225	0	1
	AB	0.966	0.225	0.850	0.225	0	1
	BCG	0	1	0.866	0.225	0.866	0.225
	ABC	0.956	0.225	0.956	0.225	0.956	0.225
F2	BG	0	1	0.594	0.213	0	1
	AB	0.938	0.225	0.894	0.225	0	1
	BCG	0	1	0.881	0.225	0.863	0.225
	ABC	0.975	0.225	0.975	0.225	0.975	0.225
F3	BG	0	1	0.916	0.200	0	1
	AB	0.900	0.225	0.894	0.225	0	1
	BCG	0	1	0.900	0.225	0.906	0.200
	ABC	0.956	0.225	0.956	0.225	0.956	0.225

C. Robustness to Nonideal Conditions

Various nonideal conditions such as CT errors, saturation, and outliers consistently threaten the security of differential protection. Therefore, we evaluate the ability of the proposed protection method to withstand various nonideal conditions. For this purpose, bus 33 is subjected to a bolted ABG fault considering CT errors, saturation, and outliers. The simulation results are shown in Fig. 11(a)-(c).

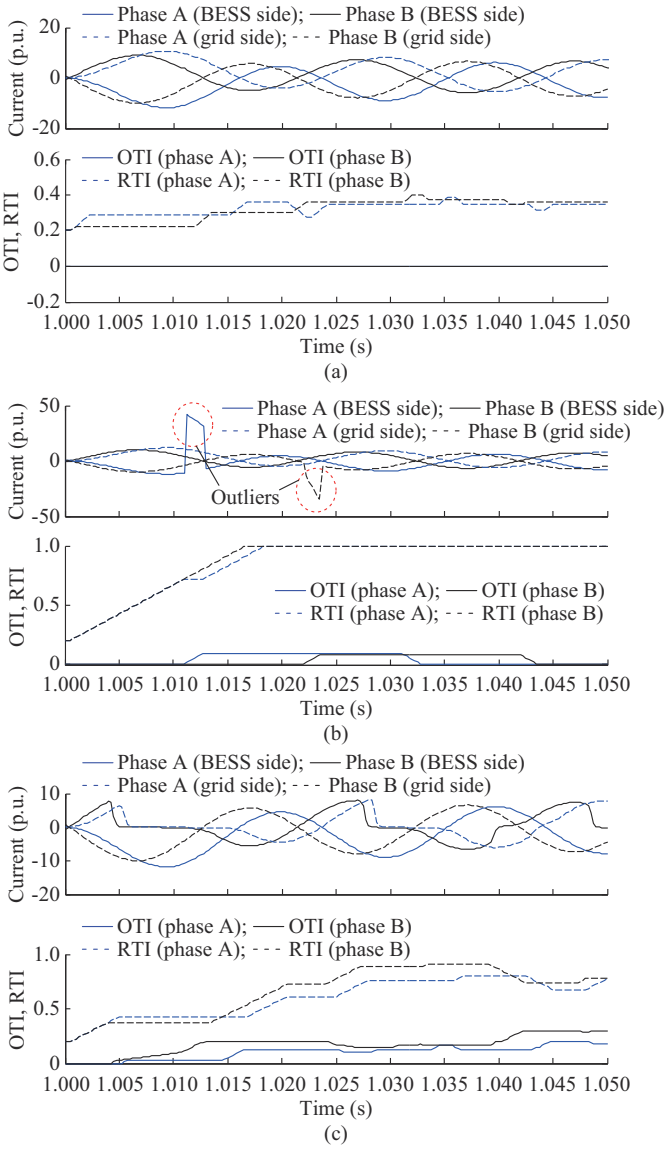

Fig. 11. Simulation results under various nonideal conditions. (a) CT error. (b) Outliers. (c) CT saturation.

For the scenario corresponding to Fig. 11(a), the CT of phase A on the grid side has a −10% measurement error, while CT of phase B on the BESS side has a −10% measurement error. For the scenario corresponding to Fig. 11(b), outliers are concurrently introduced into both the phase-A current on the BESS side and phase-B current on the grid side. For the scenario corresponding to Fig. 11(c), the CTs of phase A on the grid side and phase B on the BESS side are saturated. The OTI and RTI shown in Fig. 11(a)-(c) indicate that the OTI values remain noticeably smaller than the RTI values. Thus, the faults are accurately identified as external faults. This signifies that the proposed protection method makes correct decisions without mistakenly issuing trip signals, demonstrating robustness against CT errors, saturation, and outliers.

D. Effect of BESS Capacity

To assess the tolerance of the proposed protection method to the BESS capacity, AG faults with a fault resistance of 100 Ω are introduced at the midpoint of line 33-19 under different BESS capacities of 150 MW, 250 MW, and 350 MW. Moreover, the charging and discharging states of the BESS are considered. The waveforms of the OTI and RTI under different BESS capacities are shown in Fig. 12(a)-(c). Regardless of the variations in the BESS capacity, the OTI consistently maintains a notably larger magnitude than the RTI. According to the criterion given by (26), this indicates that the proposed protection method accurately identifies internal faults with high sensitivity for various BESS capacities.

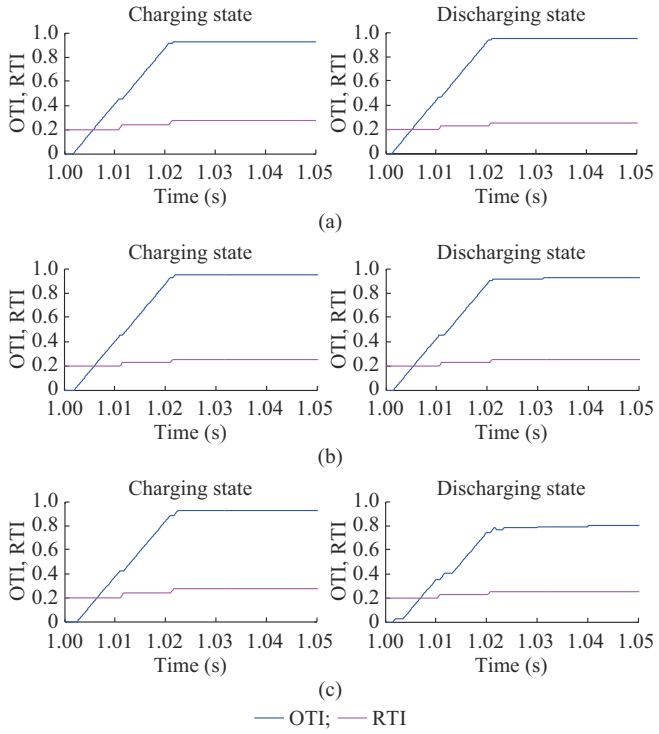

Fig. 12. Performance evaluation under different BESS capacities. (a) 150 MW. (b) 250 MW. (c) 350 MW.

E. Tolerance to Line Capacitive Current

An AG fault is applied at bus 33, which is an external fault. The BESS capacity is set to be 250 MW, and BESS operates in the charging state. The tolerance of the proposed protection method to line capacitive current is examined by considering different line lengths of 50 km, 100 km, 200 km, and 300 km.

The line capacitive currents and waveforms of the OTI and RTI with different line lengths are shown in Fig. 13(a)-(e). As shown in Fig. 13(a), with the increase of line length, the amplitude of the line capacitive current increases. As shown in Fig. 13(b)-(e), despite the substantial variations in the line length, the OTI consistently remains noticeably smaller than the RTI. Hence, the fault is consistently and accurately identified as an external fault regardless of the line length. The proposed protection method exhibits remarkable tolerance to the line capacitive current.

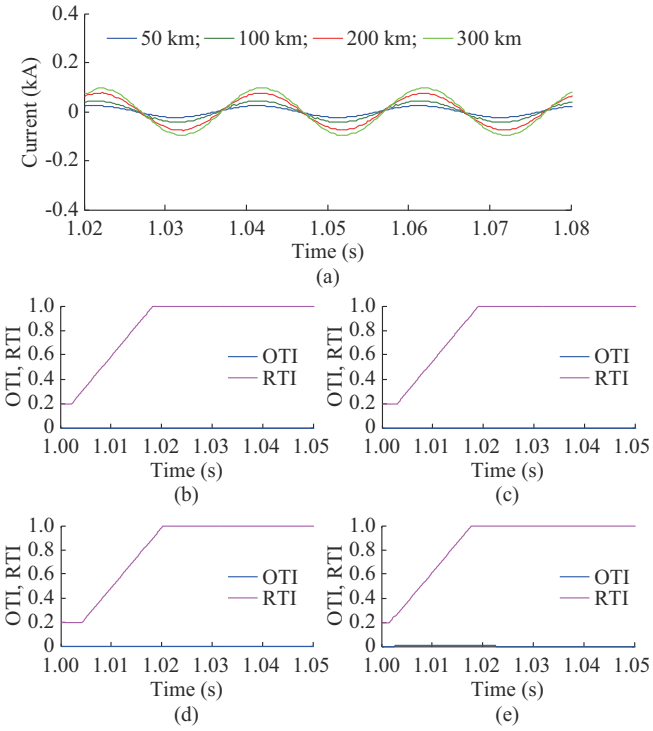

Fig. 13. Line capacitive currents and waveforms of OTI and RTI with different line lengths. (a) Line capacitive current. (b) 50 km. (c) 100 km. (d) 200 km. (e) 300 km.

V. Performance Evaluation in HIL Testing Platform

To further ensure the meliority of proposed protection method, an HIL testing platform is set up in a laboratory, as shown in Fig. 14. The HIL platform includes waveform display, personal computer, serial communication channel, and relay protection testing device [22]. The protection methods are coded in C language and executed on a digital signal processor (DSP) chip of the relay protection testing device. A BESS with a capacity of 300 MW is connected to power grid using a 230 kV 30 km line. The line parameters are available in [17].

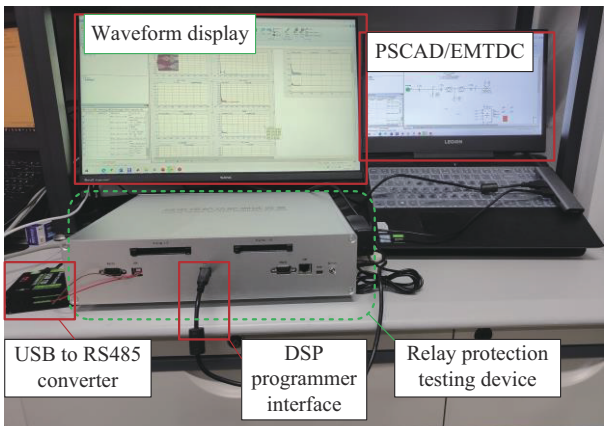

Fig. 14. HIL testing platform for relay protection.

A. Performance Evaluation in Diverse Fault Scenarios

The performance of the protection method is assessed by

considering diverse fault scenarios, which are created by changing fault distances, resistances, types, and operating states. Fault distance indicates the distance between the fault point and BESS. The results of OTI and RTI in diverse fault scenarios are listed in Table II. The OTI is consistently much larger than the RTI for faulty phases, whereas it is consistently much smaller than the RTI for healthy phases. Therefore, regardless of the variations in fault types, resistances, distances, and operating states, the proposed protection method consistently performs accurate decision-making.

TABLE II
RESULTS OF OTI AND RTI IN DIVERSE FAULT SCENARIOS

Operating state	Fault type	Fault distance (km)	Fault resistance (Ω)	Phase A		Phase B		Phase C	
				OTI	RTI	OTI	RTI	OTI	RTI
Charging state	**AB (case 1)**	**1**	**1**	0.781	0.200	0.791	0.200	0	1
	ABC	10	25	0.975	0.225	0.981	0.200	0.956	0.225
	BCG	20	50	0	1	0.938	0.225	0.938	0.225
	BG	29	100	0	1	0.950	0.250	0	1
Discharging state	AB	1	1	0.894	0.200	0.741	0.200	0	1
	ABC	10	25	1	0.200	0.966	0.225	0.981	0.200
	BCG	20	50	0	1	0.956	0.225	0.956	0.225
	BG (case 2)	**29**	**100**	0	1	0.925	0.250	0	1

The results corresponding to cases 1 and 2 highlighted in bold in Table II are shown in Figs. 15 and 16, respectively.

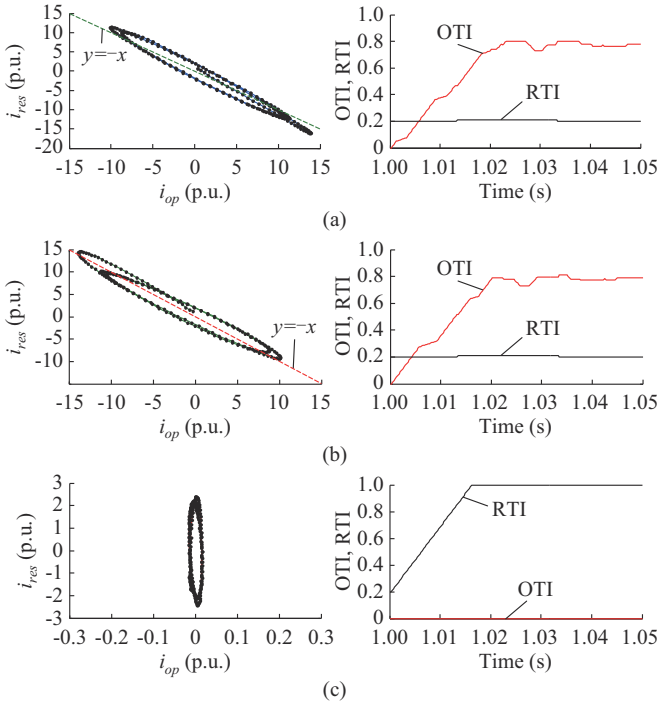

Fig. 15. Results of case 1. (a) Phase A. (b) Phase B. (c) Phase C.

In Fig. 15, the fault resistance (1 Ω) is very small, so the trajectories of the faulty phases (phases A and B) are close to $y=-x$, while the trajectory of healthy phase (phase C) is adjacent to y-axis ($x=0$). This result is entirely consistent with the analysis presented in Section III. Consequently, the OTIs of phases A and B are considerably greater than the corresponding RTIs, whereas the opposite holds true for phase C. Thus, the proposed protection method can function accurately.

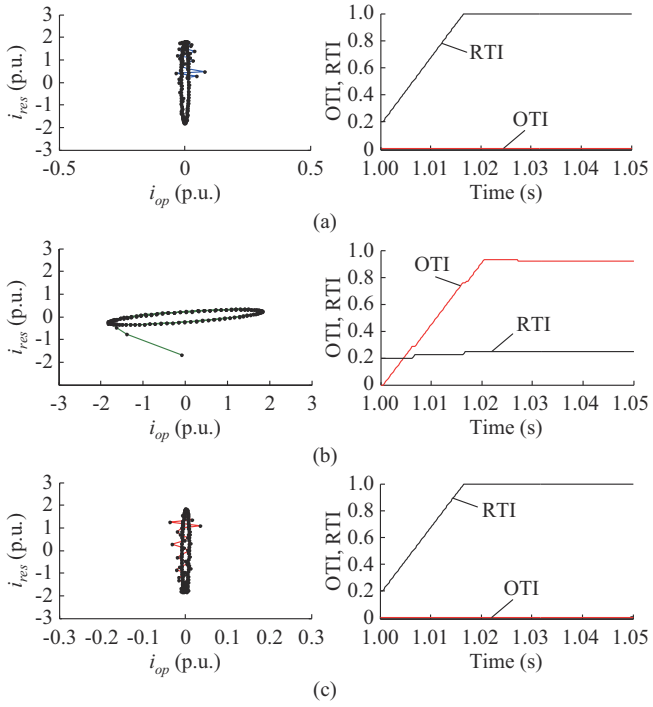

Fig. 16. Results of case 2. (a) Phase A. (b) Phase B. (c) Phase C.

The current trajectories and waveforms of the OTI and RTI for case 2 are depicted in Fig. 16. The OTI of phase B substantially surpasses the RTIs, whereas phases A and C exhibit the opposite trend. In case 2, the proposed protection method can also function accurately. Additionally, for the faulty phase, the protection criterion is always fulfilled within 10 ms after the fault occurrence, indicating a rapid response speed.

B. Comparison with State-of-the-art TDDP Methods

To highlight the superiority of the proposed protection method, it is compared with three state-of-the-art TDDP

methods, i.e., CSC-based TDDP (CSC-TDDP) [11], fault detection index based TDDP (FDI-TDDP) [13], and current trajectory coefficient based TDDP (CTC-TDDP) [19].

1) Internal Fault

An AG fault with a fault resistance of 100 Ω occurs at a distance of 10 km from the BESS. Figure 17(a)-(d) shows the results obtained for phase A using the four protection methods.

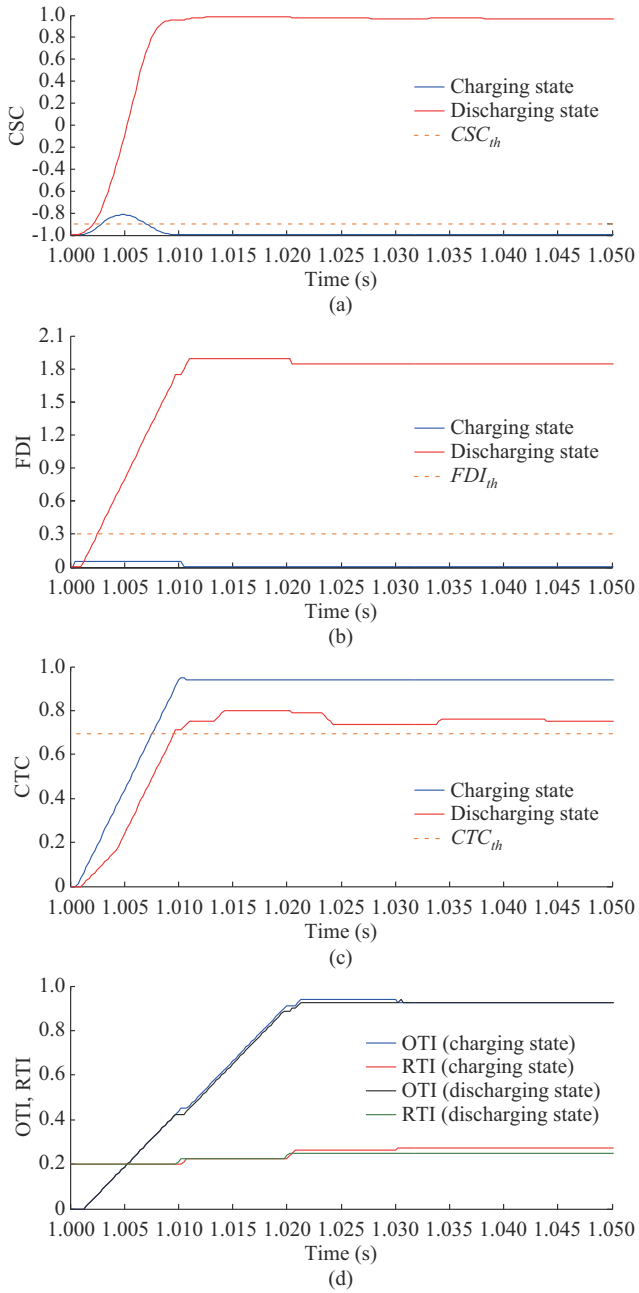

Fig. 17. Comparison of four protection methods under internal fault. (a) CSC-TDDP. (b) FDI-TDDP. (c) CTC-TDDP. (d) Proposed protection method.

From Fig. 17(a), the CSC-TDDP exhibits completely different behaviors in the charging and discharging states. In the discharging state, the CSC-TDDP substantially exceeds the threshold CSC_{th}. However, in the charging state, the CSC-TDDP slightly exceeds the threshold in the transient state and falls below the threshold in the steady state. It signifies that CSC-TDDP demonstrates a low level of sensitivity and bears the risk of rejection in the charging state. According to Fig. 17(b), the FDI-TDDP surpasses the threshold FDI_{th} by a considerable amount in the discharging state, but remains below FDI_{th} in the charging state. Similar to CSC-TDDP, FDI-TDDP exhibits a distinctively superior performance in the discharging state than in the charging state. Likewise, FDI-TDDP also faces the potential for rejection in the charging state. As observed from Fig. 17(c), the CTC-TDDP consistently exceeds the threshold CTC_{th} regardless of the charging or discharging state. Nevertheless, the CTC-TDDP remains slightly higher than CTC_{th} in the discharging state, indicating a low sensitivity. As shown in Fig. 17(d), in both the charging and discharging states, the OTI consistently exhibits a markedly higher value than the RTI. Thus, the proposed protection method can always operate correctly and sensitively.

2) External Fault

A comparative study on the robustness to CT saturation of the four protection methods is also necessary. To do this, an external AG fault with a fault resistance of 0 Ω is applied, and the CT on the grid side is set to be the saturation mode. The BESS operates in the charging state. Figure 18(a)-(d) illustrates the results obtained for phase A using the four protection methods. As shown in Fig. 18(a) and (b), due to CT saturation, both CSC-TDDP and FDI-TDDP exhibit substantial deviations beyond their respective thresholds. Consequently, the CSC-TDDP and FDI-TDDP misidentify this fault as being inside the protection zone and erroneously generate trip signals. From Fig. 18(c) and (d), the CTC is below its threshold CTC_{th}, while the OTI is less than the RTI. It is clear that CTC-TDDP and the proposed protection method display a much higher level of robustness to CT saturation than the CSC-TDDP and FDI-TDDP.

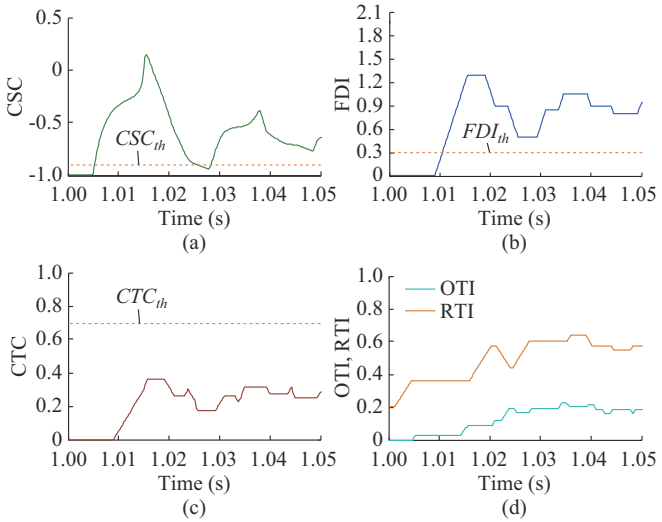

Fig. 18. Comparison of four TDDP methods under external faults with CT saturation. (a) CSC-TDDP. (b) FDI-TDDP. (c) CTC-TDDP. (d) Proposed protection method.

According to the above-mentioned analysis, CTC-TDDP and the proposed protection method demonstrate higher dependability than the CSC-TDDP and FDI-TDDP in different operating states. However, the proposed protection method outperforms CTC-TDDP in terms of sensitivity. In addition, compared with CSC-TDDP and FDI-TDDP, CTC-TDDP and the proposed protection method also exhibit superior security in the presence of CT saturation. Overall, compared with other three TDDP methods, the proposed protection method exhibits increased dependability, sensitivity, and security.

VI. Discussion

Modern power systems are gradually evolving toward new power systems dominated by power electronic-based sources, including renewable energy sources, VSC-HVDC stations, and BESSs, etc. This profoundly alters the fault characteristics of the power system, deteriorates the operating performance of relay protection, and poses a threat to the safety of the power system. Most studies focus on studying the fault characteristics of certain power electronic-based sources and exploring protection principles that match these characteristics. However, the differing fault characteristics between different types of power electronic-based sources make the existing protection principles less universally applicable.

Thus, conducting in-depth research on the common characteristics of various types of power electronic-based sources and devising novel protection principles that can adapt to various types of power electronic-based sources may be more well-received. Additionally, exploring new protection methods that do not rely on the fault characteristics of power sources is also an emerging research trend.

Deep learning may be useful to address problems in relay protection. Integrating state-of-the-art deep learning algorithms with relay protection may produce remarkable results beyond the initial expectations. However, the interpretability of deep learning based data-driven protection methods is poor. In future work, deep learning can be merged with expert knowledge to develop a new protection method driven by a combination of knowledge and data to ensure high accuracy while improving interpretability.

VII. Conclusion

In response to the challenges posed by the integration of BESSs in both conventional CDP and newly-proposed TDDP methods, we account for the trajectory distribution discrepancy to propose a new time-domain CDP method based on the OTI and RTI. An extensive performance evaluation of the proposed protection method and comparative study with state-of-the-art TDDP methods are conducted using PSCAD simulations and an HIL testing platform. The findings of this study are summarized as follows.

1) Compared with the discharging state, the effectiveness of CDP is more likely to be compromised in the charging state of BESS. Conventional CDP is highly resilient to CT errors, but its security may be reduced, leading to false trip signals in the presence of CT saturation and outliers.

2) The trajectory formed by operating and restraining current samples exhibits notable variations in its distribution characteristics between internal faults and other events. This behavior is exploited to develop the proposed TDDP method that precisely identifies internal faults from other events.

3) The proposed protection method demonstrates excellent robustness to CT saturation, errors, and outliers, and it performs well across various fault types, resistances, locations, and operating states. Compared with three state-of-the-art TDDP methods, i. e., CSC-TDD, FDI-TDDP, and CTC-TDDP, the proposed protection method exhibits superior dependability, sensitivity, and security.

References

[1] F. Zheng, X. Zhou, B. Rahat *et al*., "Carbon neutrality target for leading exporting countries: on the role of economic complexity index and renewable energy electricity," *Journal of Environmental Management*, vol. 299, p. 113558, Dec. 2021.

[2] U. Datta, A. Kalam, and J. Shi, "The relevance of large-scale battery energy storage (BES) application in providing primary frequency control with increased wind energy penetration," *Journal of Energy Storage*, vol. 23, pp. 9-18, Jun. 2019.

[3] L. M. S. de Siqueira and W. Peng, "Control strategy to smooth wind power output using battery energy storage system: a review," *Journal of Energy Storage*, vol. 35, p. 102252, Mar. 2021.

[4] Z. Guo, W. Wei, L. Chen *et al*., "Impact of energy storage on renewable energy utilization: a geometric description," *IEEE Transactions on Sustainable Energy*, vol. 12, no. 2, pp. 874-885, Apr. 2021.

[5] A. N. R. L. Sirisha and A. K. Pradhan, "Subcycle transmission line protection using time-domain similarity measure," *International Journal of Electrical Power & Energy Systems*, vol. 137, p. 107766, May 2022.

[6] L. Chen, X. Lin, Z. Li *et al*., "Similarity comparison based high-speed pilot protection for transmission line," *IEEE Transactions on Power Delivery*, vol. 33, no. 2, pp. 938-948, Apr. 2018.

[7] S. Chen, N. Tai, C. Fan *et al*., "Sequence-component-based current differential protection for transmission lines connected with IIGs," *IET Generation*, *Transmission & Distribution*, vol. 12, no. 12, pp. 3086-3096, Jul. 2018.

[8] H. Gao, J. Li, and B. Xu, "Principle and implementation of current differential protection in distribution networks with high penetration of DGs," *IEEE Transactions on Power Delivery*, vol. 32, no. 1, pp. 565-574, Feb. 2017.

[9] G. Chen, Y. Liu, and Q. Yang, "Impedance differential protection for active distribution network," *IEEE Transactions on Power Delivery*, vol. 35, no. 1, pp. 25-36, Feb. 2020.

[10] K. Jia, Y. Li, Y. Fang *et al*., "Transient current similarity based protection for wind farm transmission lines," *Applied Energy*, vol. 225, pp. 42-51, Sept. 2018.

[11] L. Zheng, K. Jia, T. Bi *et al*., "Cosine similarity based line protection for large-scale wind farms," *IEEE Transactions on Industrial Electronics*, vol. 68, no. 7, pp. 5990-5999, Jul. 2021.

[12] L. Zheng, K. Jia, W. Wu *et al*., "Cosine similarity based line protection for large scale wind farms part II – the industrial application," *IEEE Transactions on Industrial Electronics*, vol. 69, no. 3, pp. 2599-2609, Mar. 2022.

[13] A. Saber, M. F. Shaaban, and H. H. Zeineldin, "A new differential protection algorithm for transmission lines connected to large-scale wind farms," *International Journal of Electrical Power & Energy Systems*, vol. 141, p. 108220, Oct. 2022.

[14] Z. Yang, W. Liao, H. Wang *et al*., "Improved euclidean distance based pilot protection for lines with renewable energy sources," *IEEE Transactions on Industrial Informatics*, vol. 18, no. 12, pp. 8551-8562, Dec. 2022.

[15] A. Saber, H. H. Zeineldin, T. H. M. El-Fouly *et al*., "A signed correlation index-based differential protection scheme for inverter-based islanded microgrids," *International Journal of Electrical Power & Energy Systems*, vol. 145, p. 108721, Feb. 2023.

[16] Y. Liang, Y. Ren, and W. He, "An enhanced current differential protection for AC transmission lines connecting MMC-HVDC stations," *IEEE Systems Journal*, vol. 17, no. 1, pp. 892-903, Mar. 2023.

[17] Y. Liang, Y. Ren, and Z. Zhang, "Pilot protection based on two-dimensional space projection of dual differential currents for lines connect-

ing MMC-HVDC stations," *IEEE Transactions on Industrial Electronics*, vol. 70, no. 5, pp. 4356-4368, May 2023.
[18] A. M. Joshua and K. P. Vittal, "Protection schemes for a battery energy storage system based microgrid," *Electric Power Systems Research*, vol. 204, p. 107701, Mar. 2022.
[19] Y. Liang, X. Yang, Y. Wang *et al*., "Internal fault probability-based time domain differential protection applied to transmission lines connecting battery energy storage stations," *Journal of Energy Storage*, vol. 55, p. 105707, Nov. 2022.
[20] Y. Liang, C. Pan, and J. Zhang, "Current trajectory coefficient based time domain line protection for battery storage energy stations," *Journal of Energy Storage*, vol. 51, p. 104468, Jul. 2022.
[21] M. Hossain, I. Leevongwat, and P. Rastgoufard, "Revisions on alpha plane for enhanced sensitivity of line differential protection," *IEEE Transactions on Power Delivery*, vol. 33, no. 6, pp. 3260-3262, Dec. 2018.
[22] J. R. Camarillo-Peñaranda, M. Aredes, and G. Ramos, "Hardware-in-the-loop testing of a distance protection relay," *IEEE Transactions on Industry Applications*, vol. 57, no. 3, pp. 2326-2331, May 2021.

Yingyu Liang received the B.S. degree in electrical engineering and its automation from Northeast Electric Power University, Jilin, China, in 2011, and the Ph.D. degree in power system and its automation from North China Electric Power University, Beijing, China, in 2016. He is currently an Associate Professor with China University of Mining and Technology (Beijing), Beijing, China. His research interests include protection and control of new power systems.

Cunyue Pan received the B.S. degree in electrical engineering and its automation from Shandong University of Technology, Zibo, China, in 2021. He is currently pursuing the Ph. D. degree in electrical engineering in China University of Mining and Technology (Beijing), Beijing, China. His research interests include protection and control of new power systems.